PHYSICAL REVIEW B, VOLUME 65, 064419

Mössbauer diffractometry on polycrystalline $^{57}Fe_3Al$

B. Fultz, T. A. Stephens, J. Y. Y. Lin, and U. Kriplani
California Institute of Technology, W. M. Keck Laboratory, mail 138-78, Pasadena, California 91125

(Received 7 August 2001; published 16 January 2002)

A Mössbauer powder diffractometer was used to measure diffraction patterns from polycrystalline foils of $^{57}Fe_3Al$. The intensities of Bragg diffractions were measured as a function of the energy of the incident photon. The bcc fundamental diffractions showed large changes in intensity as the incident energy was tuned through the nuclear resonances. These variations of diffraction intensity with incident energy were calculated with reasonable success using a kinematical theory of diffraction that included effects of coherent interference between x-ray Rayleigh scattering and, more importantly for these samples, Mössbauer scattering from nuclei having different hyperfine magnetic fields.

DOI: 10.1103/PhysRevB.65.064419 PACS number(s): 76.80.+y, 61.18.Fs, 61.10.−i

I. INTRODUCTION

Experimental evidence for coherent interference between Mössbauer scattering and x-ray Rayleigh scattering was found first in an experiment by Black and Moon,[1] in which a Mössbauer energy spectrum was measured in scattering geometry. The coherent interference between Mössbauer scattering and x-ray Rayleigh scattering undergoes a change from constructive in-phase interference above the Mössbauer resonance to destructive out-of-phase interference below. This gives an asymmetry to the peaks measured in an energy spectrum. There have been many other studies of coherent interference in Mössbauer scattering.[2–9] In almost all of these studies, a detector was placed at a few angles near a Bragg peak, and an energy spectrum was measured. This was the method used in experiments by Kovalenko *et al.*[10] and Nakai *et al.*[11,12] who measured interference effects between Mössbauer nuclei having different hyperfine fields.

Measurements of Mössbauer diffraction patterns, as opposed to Mössbauer energy spectra, are challenging for technical reasons. Since the first Mössbauer diffraction experiments by Black and Duerdoth,[13] there have been a number of review articles covering the subject of Mössbauer diffraction[14–20] and related topics.[21–25] Nearly all this work has used high-quality single crystals to maximize diffracted intensities, requiring interpretation by dynamical diffraction theory[14–16,26–33] instead of kinematical theory.[2,3,14–16] Diffraction data acquired in dynamical conditions (multiple scattering) are impractical to invert to obtain spatial information about the scatterers in the crystals, especially when the crystals are imperfect. Quantification of diffraction intensities with kinematical theory is an advantage in principle of performing Mössbauer diffraction experiments on polycrystalline samples. Mössbauer powder diffraction patterns have not been obtained until recently, however,[34] owing to the low intensities of the diffraction peaks.

In this paper we present a kinematical diffraction theory for both Mössbauer and x-ray Rayleigh scattering. The theory also considers coherent interference between the Mössbauer scatterings from different nuclear resonances, a typical situation when nuclear transitions have similar energies. The kinematical diffraction theory is tested with data from a Mössbauer powder diffractometer with polycrystalline samples of a partially ordered alloy of $^{57}Fe_3Al$. This material is convenient because its hyperfine magnetic fields (HMF) are large, giving a good spread of the different nuclear energy levels, and this HMF distribution is understood well, facilitating the interpretation of the coherent interferences between the scattering from different nuclei in the sample. The intensities of fundamental Bragg diffractions from the sample showed a strong dependence on the Doppler velocity of the radiation source. With the HMF distribution measured by conventional conversion electron Mössbauer spectrometry, the kinematical theory was used to calculate the intensities of the diffraction peaks for different energies of incident photons. We found reasonable agreement between the experimental and calculated intensities. Although coherent interference between x-ray Rayleigh scattering and Mössbauer scattering was important, the largest effects of coherent interference for $^{57}Fe_3Al$ were shown to originate primarily with the interference between Mössbauer scatterings from ^{57}Fe nuclei in different chemical environments.

II. THEORY

The photon wave scattered by an atom at $\vec{r}_i$ includes contributions from both Mössbauer (nuclear) and x-ray (electron) scattering. The form factors for these two coherent scattering processes are added to produce a coherent scattered wavelet ψ_i, with the amplitude and relative phase:

$$\psi_i(\vec{r}_i,\overrightarrow{\Delta k},\delta\varepsilon_i^l)=e^{-i\overrightarrow{\Delta k}\cdot\vec{r}_i}[f_X(\vec{r}_i)+f_M(\vec{r}_i,\delta\varepsilon_i^l)], \tag{1}$$

where

$$\delta\varepsilon_i^l=E-\varepsilon_i^l. \tag{2}$$

Here E is the precise energy of the incident γ-ray. The energy of the lth transition of the nucleus at $\vec{r}_i$ is ε_i^l. Here l denotes the transition within the nucleus. For ^{57}Fe in the ferromagnetic samples used here, there are six allowed nuclear transitions, so $1\leqslant l\leqslant 6$. Each atom may have a different chemical environment, so the atom at $\vec{r}_i$ may have a unique $\delta\varepsilon_i^l$. The diffraction vector $\overrightarrow{\Delta k}$ is defined in the usual way:[35]

$$\overrightarrow{\Delta k}\equiv\vec{k}-\vec{k}_0, \tag{3}$$

where the wave vector of the scattered wave is $\vec{k}$, and the incident wave vector is $\vec{k}_0$.

The total diffracted wave $\psi(\overrightarrow{\Delta k},E)$ is the sum of the $\psi_i(\vec{r}_i,\overrightarrow{\Delta k},\delta\varepsilon_i^l)$ for atoms at all $\vec{r}_i$:

$$\psi(\overrightarrow{\Delta k},E)=\sum_{\vec{r}_i} e^{-i\overrightarrow{\Delta k}\cdot\vec{r}_i}\left[f_X(\vec{r}_i)+\sum_{l} f_M(\vec{r}_i,\delta\varepsilon_i^l)\right]. \tag{4}$$

The intensity $I(\overrightarrow{\Delta k},E)$ of the diffracted wave is

$$I(\overrightarrow{\Delta k},E)=\psi(\overrightarrow{\Delta k},E)\,\psi^*(\overrightarrow{\Delta k},E), \tag{5}$$

$$I(\overrightarrow{\Delta k},E)=\sum_{\vec{r}_i} e^{-i\overrightarrow{\Delta k}\cdot\vec{r}_i}\left[f_X(\vec{r}_i)+\sum_{l=1}^{6} f_M(\vec{r}_i,\delta\varepsilon_i^l)\right] \times\sum_{\vec{r}_j} e^{i\overrightarrow{\Delta k}\cdot\vec{r}_j}\left[f_X^*(\vec{r}_j)+\sum_{l=1}^{6} f_M^*(\vec{r}_j,\delta\varepsilon_j^l)\right], \tag{6}$$

$$I(\overrightarrow{\Delta k},E)=\sum_{\vec{r}_i}\sum_{\vec{r}_j} e^{-i\overrightarrow{\Delta k}\cdot(\vec{r}_i-\vec{r}_j)}\Bigg\{f_X(\vec{r}_i)f_X^*(\vec{r}_j)+f_X(\vec{r}_i)\times\left[\sum_{l=1}^{6} f_M^*(\vec{r}_j,\delta\varepsilon_j^l)\right]+\left[\sum_{l=1}^{6} f_M(\vec{r}_i,\delta\varepsilon_i^l)\right]f_X^*(\vec{r}_j)+\sum_{l=1}^{6}\sum_{l'=1}^{6} f_M(\vec{r}_i,\delta\varepsilon_i^l)f_M^*(\vec{r}_j,\delta\varepsilon_j^{l'})\Bigg\}. \tag{7}$$

With the definition

$$\vec{R}\equiv\vec{r}_i-\vec{r}_j, \tag{8}$$

$$I(\overrightarrow{\Delta k},E)=\sum_{\vec{R}} e^{-i\overrightarrow{\Delta k}\cdot\vec{R}}\{\mathcal{P}_{XX}(\vec{R})+\mathcal{P}_{XM}(\vec{R},E)+\mathcal{P}_{MX}(\vec{R},E)+\mathcal{P}_{MM}(\vec{R},E)\}, \tag{9}$$

where we have defined the four Patterson functions

$$\mathcal{P}_{XX}(\vec{R})\equiv\sum_{\vec{r}}\overline{f_X(\vec{r})f_X^*(\vec{r}+\vec{R})}=\sum_{\vec{r}} f_X(\vec{r})f_X^*(\vec{r}+\vec{R}), \tag{10}$$

$$\mathcal{P}_{XM}(\vec{R},E)\equiv\sum_{\vec{r}}\sum_{l=1}^{6}\overline{f_X(\vec{r})f_M^*(\vec{r}+\vec{R},\delta\varepsilon_i^l)}=\sum_{\vec{r}}\sum_{l=1}^{6} f_X(\vec{r})\overline{f_M^*(\vec{r}+\vec{R},\delta\varepsilon_i^l)}, \tag{11}$$

$$\mathcal{P}_{MX}(\vec{R},E)\equiv\sum_{\vec{r}}\sum_{l=1}^{6}\overline{f_M(\vec{r},\delta\varepsilon_i^l)f_X^*(\vec{r}+\vec{R})}=\sum_{\vec{r}}\sum_{l=1}^{6}\overline{f_M(\vec{r},\delta\varepsilon_i^l)}f_X^*(\vec{r}+\vec{R}), \tag{12}$$

$$\mathcal{P}_{MM}(\vec{R},E)\equiv\sum_{\vec{r}}\sum_{l=1}^{6}\sum_{l'=1}^{6}\overline{f_M(\vec{r},\delta\varepsilon_i^l)f_M^*(\vec{r}+\vec{R},\delta\varepsilon_j^{l'})}. \tag{13}$$

The overlines in Eqs. (10)–(13) denote averaging over all orientations of the HMF, where the magnetic dipole polarization factors for γ-ray emission depend on these orientations, photon polarizations, and scattering angles. For x-ray processes this involves a simple dependence on $\overrightarrow{\Delta k}$. If $I(\overrightarrow{\Delta k},E)$ originated entirely from x-ray scattering, it would include a simple Lorentz-polarization factor, for example. The polarization factor for an individual nuclear resonant scattering can be shown to depend on the orientation relationship $\vec{h}\cdot\vec{u}$ for both the incident and outgoing photons, where $\vec{h}$ is the magnetic polarization of the photon and $\vec{u}_l$ is the spherical unit vector for the lth nuclear transition.[37] We write the polarization factors in abbreviated form as $P_{ll',\mathrm{nuc}}(\nu_f,\vec{k}_f,\vec{u},\nu_i,\vec{k}_i)$. Here $\overline{P_{ll',\mathrm{nuc}}}$ is the average of the angular dependence of f_M over directions of the hyperfine magnetic fields, and $\overline{P^2_{ll',\mathrm{nuc}}}$ is the orientational average of the angular dependence of $f_M f_M^*$. These $\overline{P_{ll',\mathrm{nuc}}}$ and $\overline{P^2_{ll',\mathrm{nuc}}}$ have been calculated for an unpolarized incident photon beam and isotropic[12] and anisotropic[38] hyperfine magnetic field orientation distributions. The results for an anisotropic case with a bias of HMF's in the plane of the sample did not differ substantially from the isotropic case. We therefore used the results for the isotropic case, which were the same as reported by Nakai *et al.*[12] (Their $\overline{V_{ll'}}$ are equivalent to our $\overline{P^2_{ll',\mathrm{nuc}}}$, although anisotropic $\overline{P^2_{ll',\mathrm{nuc}}}$ have only been calculated for $l=l'$.) A few of the Nakai *et al.* polarization factors were also confirmed by Monte Carlo simulations with individual scattering processes, and by numerical averaging of uniform distribution functions.

Note that $\mathcal{P}_{XX}(\vec{R})$ of Eq. (10) is the well-known Patterson function for x-ray diffraction.[36] The Patterson functions $\mathcal{P}_{XM}(\vec{R},E)$ and $\mathcal{P}_{MX}(\vec{R},E)$ of Eqs. (11) and (12) are the spatial correlation functions for the coherent interference of a photon that undergoes Mössbauer scattering from an atom and x-ray scattering from an atom. Since $\mathcal{P}_{XM}(\vec{R},E)=\mathcal{P}^*_{MX}(\vec{R},E)$, the sum $\mathcal{P}_{XM}(\vec{R},E)+\mathcal{P}_{MX}(\vec{R},E)$ is a real number. This interference between x-ray scattering and Mössbauer scattering has been the subject of extensive previous studies with Mössbauer energy spectra. Since x-ray scattering is independent of *E*, it may be possible to isolate the Mössbauer scattering through energy-dependent diffraction studies. In such studies the diffracted *intensity* would be proportional to $\Sigma_{\vec{R}}e^{-i\overrightarrow{\Delta k}\cdot\vec{R}}f_M(\vec{R})$. Such diffraction experiments have therefore been proposed as a solution to the phase problem in diffraction (see, for example, Ref. 15).

The energy dependencies of the scattering factors in Eqs. (10)–(13) include the phase and amplitude information necessary to understand the interference terms. The Mössbauer scattering factor $f_M(\vec{r}_i,\delta\varepsilon_i^l)$ is

$$f_M(\vec{r}_i,\delta\varepsilon_i^l)=-\rho(\vec{r}_i,\delta\varepsilon_i^l)\frac{G_i^l}{2\,\delta\varepsilon_i^l/\Gamma+i}. \tag{14}$$

Here $\rho(\vec{r}_i,\delta\varepsilon_i^l)$ is the probability of finding an ^{57}Fe nucleus in a chemical environment with $\delta\varepsilon_i^l$ at position $\vec{r}_i$. The denominator in Eq. (14) describes the energy dependence of the phase for resonance scattering and causes f_M to be largest when $\delta\varepsilon_i^l = 0$ (at resonance). The full natural linewidth is Γ. The G_i^l includes factors affecting the Mössbauer transition probability such as spin levels, internal conversion coefficient, Clebsch-Gordan coefficients, Lamb-Mössbauer factors, and polarization factors.[15,37,39]

The x-ray scattering factor $f_X(\vec{r})$ is independent of E:

$$f_X(\vec{r},\overrightarrow{\Delta k}) = -i[f_{\rm Fe}(\overrightarrow{\Delta k})\rho_{\rm Fe}(\vec{r}_i) + f_{\rm Al}(\overrightarrow{\Delta k})\rho_{\rm Al}(\vec{r}_i)], \tag{15}$$

where $f_{\rm Fe}(\overrightarrow{\Delta k})$ and $f_{\rm Al}(\overrightarrow{\Delta k})$ contain all of the x-ray scattering information.[35] The factor $-i$ is needed to preserve the phase information of the scattered radiation when waves are summed over Fresnel zones of the wave front. Here $\rho_{\rm Fe}(\vec{r}_i)$ is the probability of finding a Fe atom at position $\vec{r}_i$, and $\rho_{\rm Al}(\vec{r}_i)$ is the probability for Al atoms.

For the case of incoherent scattering without interference, the intensities of x-ray and Mössbauer scattering are added:

$$I_{\rm total}^{\rm inc} = I_X^{\rm inc} + I_M^{\rm inc}, \tag{16}$$

$$I_X^{\rm inc} = |f_{X0}|^2, \tag{17}$$

$$I_M^{\rm inc} = \sum_{\vec{r}_i}\sum_{l=1}^{6} \rho(\vec{r}_i, \delta\varepsilon_i^l)\frac{|f_{M0}|^2}{1+(2\delta\varepsilon_i^l/\Gamma)^2}, \tag{18}$$

where $|f_{M0}|^2$ is the differential scattering cross section for Mössbauer scattering when there is no hyperfine splitting of the resonance line. The incoherent Mössbauer scattering intensity is a set of Lorentzian peaks familiar from Mössbauer spectrometry. For incoherent scattering it is often convenient to work with the ratio of Mössbauer to x-ray scattering r_{MX}:

$$r_{MX} = \frac{|f_{M0}|^2}{|f_X|^2}R, \tag{19}$$

where R is a ratio, defined as the intensity of Mössbauer scattering, averaged over a velocity interval or "bin," to the maximum intensity of Mössbauer scattering at resonance for a single-line absorber. For thicker specimens, the Mössbauer scattering tends to saturate below the surface of the specimen. An estimate of the effect of this saturation distortion on r_{MX} for our moderately thick specimens was provided by a multislice calculation described in the Appendix. The quantity $\sqrt{r_{MX}}$ was then used to correct the ratio of Mössbauer to x-ray wave interference, compared to the ratio expected from an infinitesimally-thin specimen. Owing to the deeper penetration of x rays in the sample, this correction boosted the amount of x-ray wave amplitude and the amount of interference between the Mössbauer and x-ray scatterings.

The fractional γ-ray intensity emission back from the surface of a thick sample $I(t)/I_0$ has been formulated by Bara[40] for the incoherent case as

$$\frac{I(t)}{I_0} \propto \frac{\sigma}{\mu_{\rm eff}}(1-e^{-\mu_{\rm eff}t}), \tag{20}$$

where t is the thickness of the sample and $\mu_{\rm eff} = \mu_{\rm in}\csc(\beta_{\rm in}) + \mu_{\rm out}\csc(\beta_{\rm out})$ is the "effective" inverse absorption length for the incident and outgoing photons. Here $\mu_{\rm in}$ and $\mu_{\rm out}$ are inverse absorption lengths for incident and outgoing photons, and $\beta_{\rm in}$ and $\beta_{\rm out}$ are the angles between incident and outgoing wave vectors and the sample surface. For samples much thicker than $(\mu_{\rm eff})^{-1}$, Eq. (20) becomes $I/I_0 \propto \sigma/\mu_{\rm eff}$. In the present case where absorption by Mössbauer scattering dominates over electronic absorption ($\mu_{\rm nuc}/\mu_{\rm ele} \sim 10^2 - 10^3$), the ratio of the Mössbauer scattering cross section for γ-ray reemission σ to the Mössbauer absorption coefficient $\mu_{\rm eff}$ is approximately independent of thickness. The effect of thickness distortion on the ratio $I/I_0 \propto \sigma/\mu_{\rm eff}$ is therefore relatively small for Mössbauer scattering, and was ignored in our calculations. On the other hand, owing to the dominance of nuclear absorption over electronic absorption, it is necessary to include the ratio, $R \sim 10-30$, to account for a thickness distortion of the x-ray–Mössbauer interference.

III. EXPERIMENTAL

Ingots of ^{57}Fe$_3$Al were prepared by arc-melting 95%-enriched ^{57}Fe with Al (99.999%). The 50 to 100 mg ingots were inverted and remelted to ensure homogeneity. Some ingots were shaped into disks by piston-anvil quenching with an Edmund Bühler ultrarapid quencher. Samples were then cold rolled to the desired thickness. All samples were annealed to develop $D0_3$ order by heating in vacuum for 100 h at 450 °C. The crystallite size was estimated to be 23 nm. X-ray powder diffractometry was used to show how cold rolling left a crystallographic texture in the foil specimens. The crystallographic texture was used to favor certain diffraction peaks over others. We acquired three sets of data with the specimen rotated by a 1° angle, keeping all other conditions the same, to test if large crystallites within the sample improperly skewed the intensities. Our diffraction peaks were enhanced by texture, but were without the distortion caused by a few strongly diffracting crystallites.

The chemical composition of the sample was measured with a JEOL Superprobe 733 electron microprobe, and was found to be very close to the desired 25 at. % Al. Our samples were studied by conversion electron Mössbauer spectrometry (CEMS), performed with a backscatter electron detector with flowing He-7% CH$_4$ gas, since the samples were too enriched with ^{57}Fe to allow good measurements by transmission Mössbauer spectrometry.

An overview of the diffractometer is given here. The radiation source was 145 mCi of ^{57}Co in Rh at room temperature. The source had an active area of 6 mm, but was tilted by 60° to foreshorten its effective width to 3 mm. The γ-ray beam was collimated to 1° in width with a precision-milled lead collimator. The collimator was lined with aluminum plates to suppress lead fluorescence. A large amount of lead on the sides of the collimator shielded the detector from hard contamination radiations from the source. We tested a variety of sample holders and chose 1.5 mm Plexiglas. A thin layer of vacuum grease on top of the Plexiglas suppressed the background and held the foil in place. To suppress further the background, the beam transmitted directly through the sample was blocked from entering the detector. The shape of the beam stop was found to be important, as scattering from the block can contribute to the detector background.

A Ranger Scientific MS-900 velocity transducer provided Doppler shifts for the ^{57}Co source. The multichannel scalar (MCS) internal to the MS-900 drive controller provided three functions for the Mössbauer diffraction experiment. First, the scalar gave the reference signal for the velocity waveform. Second, the scalar signal provided the synchronous router with the timing information that directed diffraction patterns into the appropriate "velocity bins," corresponding to the velocity intervals described below. Third, the MCS memory was used to acquire Mössbauer transmission spectra as needed for tuning the synchronous router. All of the on-resonance data were acquired in "region of interest" or "flyback" mode, for which we found the drive response became increasingly nonlinear as the size of the velocity window was decreased. The nonlinearity was highly repeatable, however, so we could correct for it with a careful velocity calibration.

The detector was an Inel (Instrumentation Électronique) CPS-120 large angle (120) position sensitive detector (PSD). The detector operates in a self-quenching streamer mode.[41] We varied the detector bias to optimize the signal-to-noise (S/N) ratio. A bias of 9.3 kV provided the best S/N ratio with Ar-15% C_2H_6 gas, giving an ambient background of 3.5 Hz with no radiation source present. Absorption efficiencies for some relevant photon energies were (1) Fe K x rays at 6.4 keV: 80%, (2) Mössbauer γ ray at 14.41 keV: 15%, (3) Rh K x rays at 20.2 keV: 6%, (4) Pb K x rays at 85 keV: 0.2% , and (5) ^{57}Co γ rays at 122 keV: 0.1%. We used an aluminum filter in front of the detector to suppress 99% of the 6.4 keV x rays from the sample. We also tested a gas mix containing 10% Kr. Although the efficiency was improved for 14.41 keV γ rays, the detector became much more sensitive to harder radiations, impairing the S/N ratio. Sensitivity variations across the detector caused the background to vary up and down with a period of about 4°. All data sets were measured for two different detector positions where the detector was rotated by 2.0°, and the background periodicity was largely averaged away when the two data sets were summed. Comparisons of data acquired at different detector positions also helped identify the few isolated bad points in the detector. Although the present measurements were enabled by the Inel CPS-120 detector, this detector suffers from three serious deficiencies that must be overcome if Mössbauer diffractometry is to find further applications. Its intercepted solid angle is small, it has poor detection efficiency for 14 keV γ rays, and it has no energy resolution (causing it to be sensitive to extraneous photons and 14 keV photons that had undergone Compton scattering). Detector technologies exist to overcome all these deficiencies, however.

The two signals from the matched preamplifiers were sent to a pair of analog pulse discriminators, after which one of the signals was delayed through a digital delay line. The two signals were used to start and stop a time-to-amplitude converter (TAC). The amplitude of the TAC output pulse, corresponding to the position where the photon was detected, was sent to an analog to digital (A/D) converter and memory buffer.

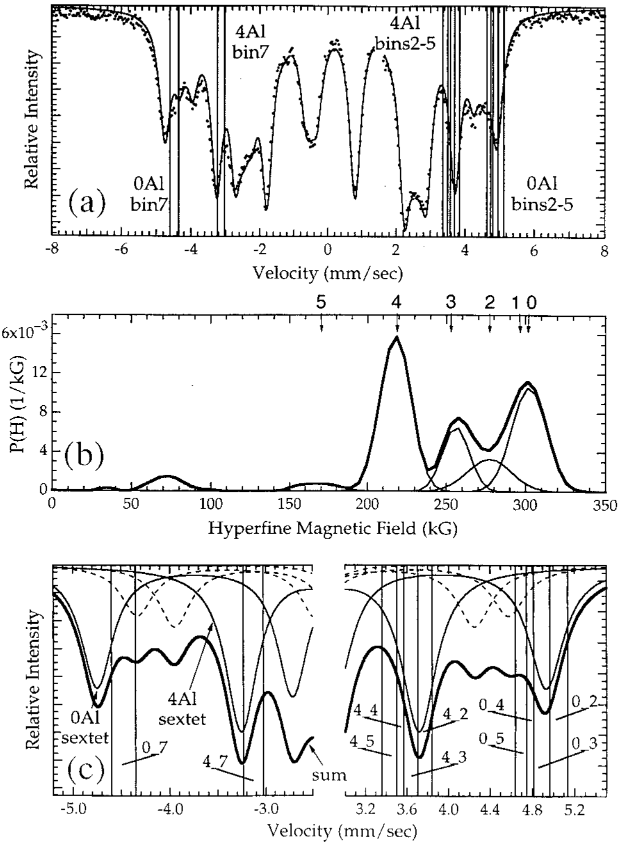

FIG. 1. (a) Conversion electron Mössbauer spectrum of annealed ^{57}Fe$_3$Al. Solid line shows reconstruction of data from HMF distribution. (b) Hyperfine magnetic field distribution from the spectrum of Fig. 2, showing Gaussian fits. The numbers at top denote the numbers of 1NN Al atom neighbors about the ^{57}Fe nucleus. (c) Enlargement of reconstruction of data from HMF distribution, showing energy bins with respect to the subpeaks from different nearest neighbor environments (the 0Al and 1Al 1NN environments were combined).

In flyback mode, the MS-900 drive was operated with velocity ranges of about three linewidths, which allowed the identification of the velocity range from the spectrum itself. An electronic means for routing the detector signals was used to select precise energy windows within this velocity range.[42] A synchronous router used the output from the MCS of the Ranger MS-900 drive controller to direct the storage of diffraction patterns into eight memory groups, or "bins," corresponding to the different velocity intervals. The component diffraction patterns and their corresponding memory groups are identified by the designation of these bins.

A conversion electron Mössbauer spectrum from the ^{57}Fe$_3$Al sample is shown in Fig. 1(a), which also shows the velocity bins when the Doppler drive was tuned to the 0Al and 4Al resonance conditions. Diffraction patterns were acquired simultaneously in the adjacent velocity bins across these two prominent resonances, and again in an

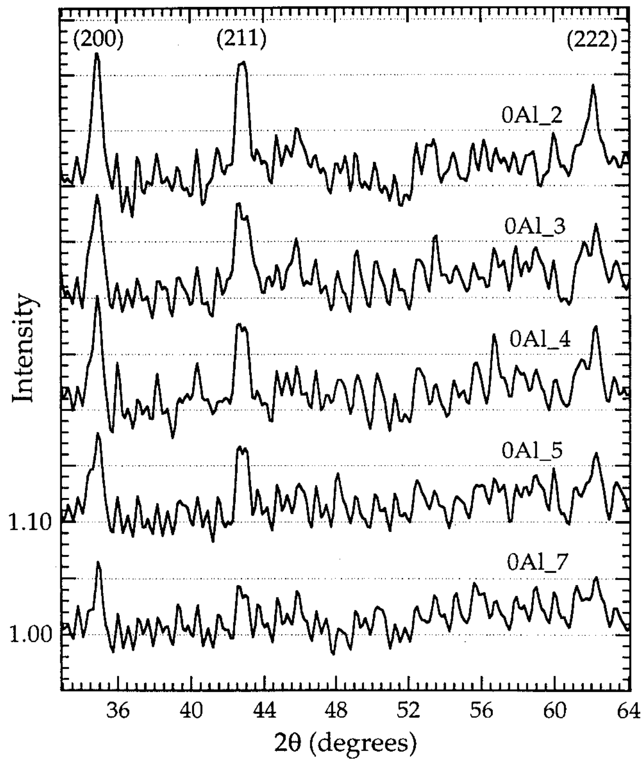

FIG. 2. Mössbauer diffraction patterns from $^{57}Fe_3Al$ for the 0Al velocity bins. Intensity is normalized to background. Diffraction patterns are offset vertically for clarity.

off-resonance condition. The off-resonance velocity bins were set for velocities greater than ±15 mm/s.

IV. RESULTS

The diffraction patterns from each of the useful velocity bins were normalized by the incident flux [source strength× collection time (in mCi h)] and were corrected by the appropriate background measurement. The counts in the background patterns (obtained without sample) were typically ten times larger than the individual diffraction patterns. Nevertheless, we found it advantageous to filter severely the high frequency Fourier components of the background before subtracting it from the individual diffraction patterns. This severe filtering suppressed nicely the statistical scatter of the background, but left some residual "ripples" in the background-corrected data. Bad points in the data were noted and removed, and the data were smoothed with a running average to eliminate an electronic problem in the MCA where the even and odd channels had slight variations in sensitivity.

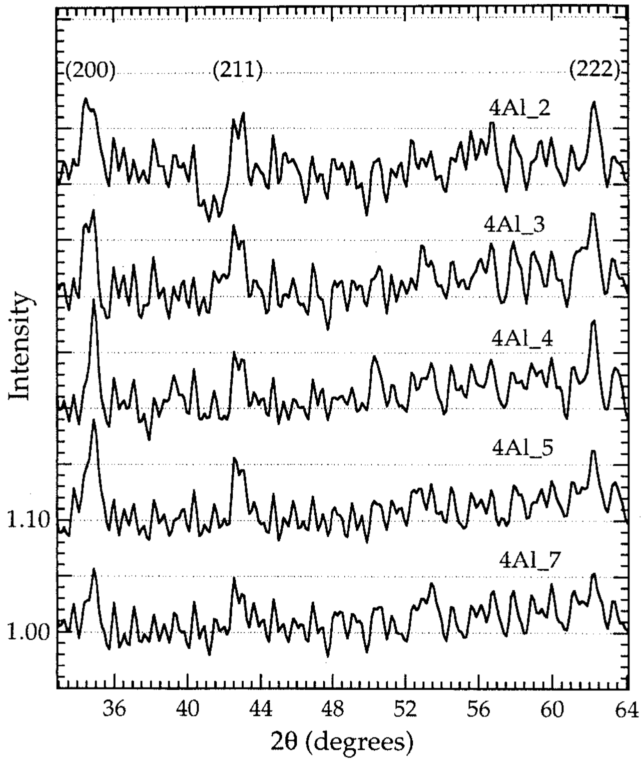

FIG. 3. Mössbauer diffraction patterns from $^{57}Fe_3Al$ for the 4Al velocity bins. Intensity is normalized to background. Diffraction patterns are offset vertically for clarity.

Figures 2 and 3 show diffraction patterns from the on-resonance velocity bins when the Doppler drive was tuned to absorption peaks from ^{57}Fe nuclei with 0Al first nearest neighbors (Fig. 2) and 4Al first nearest neighbors (Fig. 3). These data were acquired over a time and source intensity of 50,000 mCi h. The fundamental peaks (200), (211), and (222) are seen clearly, consistent with the crystallographic texture of the samples. In addition, superlattice diffractions consistent with the $D0_3$ ordered structure are seen in Fig. 2: the $(\frac{3}{2}\frac{3}{2}\frac{3}{2})$,$(\frac{5}{2}\frac{1}{2}\frac{1}{2})$ peak at 45.5° and the (300),(221) peak at 53°. The peaks of interest in the diffraction patterns were integrated numerically to obtain their intensities, which varied from about 200 to 500 counts. The statistical error was estimated by summing the total background counts within the full width at half maximum (FWHM) of the peak and taking the square root of this number. This uncertainty σ was divided into the area of the peak to obtain the peak area in units of σ. The areas of the Bragg peaks varied from 2 to 5σ.

V. CALCULATIONS OF COHERENT INTENSITIES

Mössbauer energy spectra were calculated with Eq. (9) and variants of it. From these calculations, the intensities of the diffraction peaks were obtained in the different velocity bins and compared to the experimental intensities. Only the intensities of the bcc fundamental peaks were calculated. The families of superlattice peaks, $(\frac{1}{2}\frac{1}{2}\frac{1}{2})$ and (100), had intensities that were too weak to provide statistically useful information for individual velocity bins. To identify the relative importance of the different types of coherent interference, three types of model calculations were performed: (1) no interference, as in Eq. (16), (2) interference between individual Mössbauer resonant scatterings only [obtained as the Fourier transform of $\{\mathcal{P}_{XX}(\vec{R})+\mathcal{P}_{MM}(\vec{R},E)\}$], (3) all interference effects, as in Eq. (9).

Important information for the calculations are the $\delta\varepsilon_i^l$ and $\rho(\vec{r}_i,\delta\varepsilon_i^l)$ for the different ^{57}Fe atoms. These energies and probabilities are understood well for Fe_3Al, an important reason for its selection in this experiment. The hyperfine magnetic field (HMF) distribution was obtained from the CEMS spectrum of Fig. 1(a) by the method of Le Caër and Dubois.[43] The HMF distribution provides the fractions $\rho(\vec{r}_i,\delta\varepsilon_i^l)$ [Eq. (14)], of ^{57}Fe nuclei in the various chemical environments i [Eqs. (2),(14)]. For convenience, we used the approximation that the HMF corresponds to the numbers of first-nearest-neighbor (1NN) Al atoms. This approximation is good for dilute alloys, and is even more successful for concentrated Fe-Al alloys.[44,45] The concentrations of ^{57}Fe atoms with different numbers of 1NN Al atoms were determined by fitting the HMF distribution of Fig. 1(b) to a set of Gaussian functions centered at different HMF's. The normalized intensities of the Gaussian functions were the distribution of scattering factors $\rho(\vec{r}_i,\delta\varepsilon_i^l)$ in Eq. (14). For the present analysis of fundamental diffractions of the bcc lattice, it is acceptable to set $\rho(\vec{r}_i,\delta\varepsilon_i^l)$ as the same for all bcc lattice vectors $\{\vec{r}_i\}$. Here $\delta\varepsilon_i^l$ is now considered a function of the number of 1NN Al atoms about a ^{57}Fe atom [see numbers at the top of Fig. 1(b)]. Since the 0Al and 1Al environments were not resolved experimentally, in further analysis these two environments were considered to be the same "0Al" nuclear environment. The precise velocities for the $\delta\varepsilon_i^l$ were obtained after using the HMF distribution analysis to reconstitute the measured spectrum, shown as the solid curve in Fig. 1(a). These $\delta\varepsilon_i^l$ provided positions of the Lorentzian functions shown in Figs. 1(c). The 0Al and 4Al sextets are the thin solid lines, the 2Al, 3Al, and 5Al sextets are the dashed lines, and the sum of all sextets is the thick black line.

The phase of the form factor for Mössbauer scattering is highly sensitive to $\delta\varepsilon_i^l$, and errors in these quantities contribute to errors in the calculations. The positions of isolated peaks can be determined accurately, but the errors are worse when there are peak overlaps. It should be noted that the Lorentzian functions shown in Fig. 1(c) are proportional to the square of the form factors, so the amplitudes of the waves have larger overlaps in energy than are suggested by the Lorentzian curves in Fig. 1(c). Fortunately, the crystallographic texture of the sample should not affect our results because comparisons of real and modeled data are limited to one diffraction peak at a time.

The calculated intensities were compared to the experimental intensities at eight points—the velocity bins for absorption peak 6 (bins 2–5) for the 0Al and 4Al tuning of the Doppler drive. These intensities are shown in Figs. 4 and 5. The only scaling was a normalization to set the smallest area equal to 1.0. Three curves are shown in each figure—the no interference calculation of type (1), the full calculation of type (3), and the experimental data. Figure 4 presents data for the (200) diffraction peak. Figure 5 displays data for the (211) diffraction peak for which $r_{MX}=20$.

The present analysis, based on Eq. (1), neglects effects of dynamical diffraction. The validity of the present kinematical theory could be evaluated with knowledge of the coherence lengths for diffraction. This information is, unfortunately, not available. Perhaps the best argument that dynamical effects are small is that the present theory accounts adequately for the major trends in the data. Dynamical diffraction could be responsible for some of the remaining discrepancies, however.

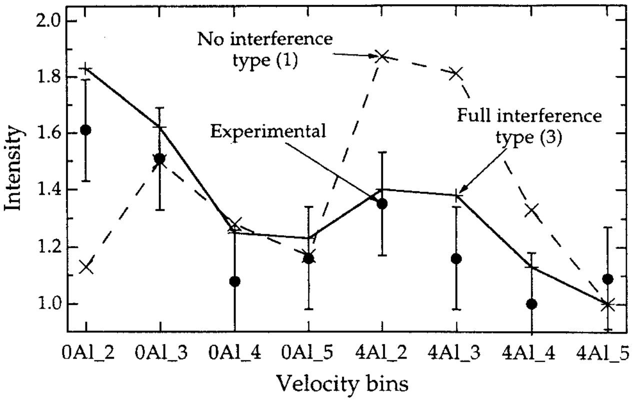

FIG. 4. Points are experimental intensities of (200) diffraction peaks from the $^{57}Fe_3Al$ sample. Lines were calculated as described in text.

VI. DISCUSSION

The most prominent difference between the diffraction patterns and the energy spectra is a qualitative change in intensities for the 0Al and 4Al environments. In the Mössbauer energy spectrum, the intensities of the peaks from the 0Al environment are weaker than those of the 4Al environment [in Fig. 1(a), the 4Al environment is at 3.6 mm/s, and the 0Al environment is at 4.6 mm/s]. This is as expected in the $D0_3$ structure, for which there are twice as many Fe atoms with 4 Al neighbors than 0 Al neighbors. In contrast, the diffraction peaks of the 0Al environment in Figs. 2, 4, 5 (especially the near-resonant bins 2 and 3) are stronger than the diffraction peaks from the 4Al environment of Figs. 3, 4, 5.

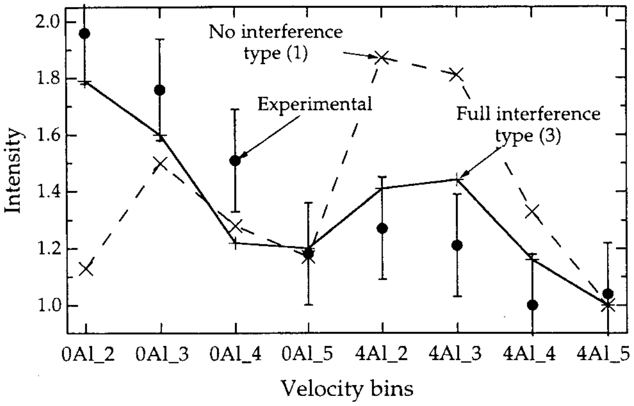

FIG. 5. Points are experimental intensities of (211) diffraction peaks from the $^{57}Fe_3Al$ sample. Lines were calculated as described in text.

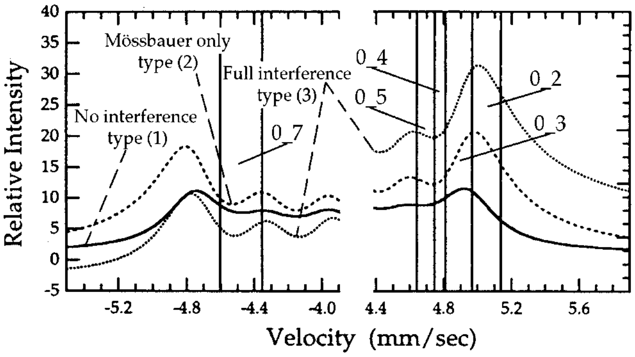

FIG. 6. Calculated energy spectra for the ^{57}Fe$_3$Al sample for the (200) diffraction. Locations of the velocity bins are indicated. The three curves are results from the three types of calculations described in Sec. V.

Most of this trend is caused by the destructive M-M interference between the low energy tail of peaks 6 of the sextet from the 3Al environment and the 4Al environment. Coherent interference between the x-ray Rayleigh scattering and Mössbauer scattering (X-M interference) further enhances the intensity of the 0Al diffraction intensity with respect to the 4Al diffraction intensity.

Other detailed effects of coherent interference are seen in Figs. 4 and 5. In another trend contrary to that of the energy spectrum, destructive interference between Mössbauer scattering from the 0Al environment and the 2Al environment (M-M interference) is primarily responsible for the intensity in velocity bin 0Al_3 being suppressed with respect to the intensity in 0Al_2. This can be understood by examining the high energy tail of the 2Al peak in Fig. 1, which overlaps more strongly with the 0Al peak in velocity bin 3 than it does in bin 2.

Towards the middle of a broad spectrum, interference tends to level the variations in diffraction intensities. There is a more gradual change in diffraction intensities for velocities across peak 6 of the 4Al sextet than is predicted without interference (bins 4Al_2, 4Al_3, 4Al_4, 4Al_5). The diffraction intensities from bins 2 and 3 are suppressed owing to M-M interference with the low energy tails of the 3Al environment. [Although the tails of the Mössbauer absorption peaks in Fig. 1(c) appear weak in the regions of overlap, the coherent interference depends on the larger amplitude and phase of the interfering wave.] There is also an enhancement in intensity at the velocities of bins 4Al_4 and 4Al_5 caused by constructive X-M interference involving the coherent part of peak 5 of the 0Al environment.

Bin 7 in Figs. 4 and 5 gave the weakest diffraction peaks of all the velocity bins. Our calculations showed a strongly suppressed intensity for velocity bin 7 (see Fig. 6). These results were consistent with calculations that showed suppressed intensity in velocity bin 7 for both the 0Al or 4Al tunings, caused by a combination of X-M and M-M destructive interferences. [The M-M destructive interference for the 0Al tuning was particularly susceptible to errors in the velocity range, since this velocity range fell between resonances from ^{57}Fe nuclei with 0 and 2 Al neighbors, and the Doppler drive was unfortunately nonlinear at negative velocities.]

For the diffractions measured in the present work, the coherent interference between Mössbauer scattering from different chemical environments (M-M) is more prominent than the coherent interference between x-ray Rayleigh scattering and Mössbauer scattering (X-M). In comparing Figs. 4 and 5, note that the difference in r_{MX} ($10R$ for Fig. 4, $20R$ for Fig. 5) has a relatively small effect on the predicted trend in intensities, and the experimental data in both figures are similar. The calculations of type (2), which neglected X-M interference but included M-M interference, provided nearly the same results in Figs. 4 and 5 as did the calculations with all effects of coherent interference. In a Mössbauer spectrum with many overlapping components, the X-M interference is both destructive and constructive. The most prominent effects of X-M interference are seen across the entire energy spectrum, where the intensity tends to be suppressed at negative velocities, and enhanced at positive velocities. This is seen by comparing the dashed and thick curves on the left and right halves of Fig. 6. Over small ranges of velocity, however, the most prominent effects are from M-M interference.

VII. CONCLUSION

We measured diffraction patterns from polycrystalline foils of ^{57}Fe$_3$Al for various energies of the incident photon. The bcc fundamental diffractions were strong, and large changes in the intensities of the Bragg diffractions were observed as the incident energy was tuned through the nuclear resonances. The variation of diffraction intensity with incident energy was consistent with a kinematical theory of diffraction that included effects of coherent interference between x-ray Rayleigh scattering and Mössbauer scattering (X-M) and Mössbauer scattering from nuclei in different chemical environments (M-M), and isotropic averages of polarization factors. For the diffraction peaks measured in the present work, the effects of M-M coherent interference were stronger than the effects of X-M interference. Because M-M interference changes from destructive to constructive over small intervals in energy, constructive interference tends to be suppressed in regions where there are many nuclear resonances separated by half a linewidth or so. The effects are large, and must be understood in order to interpret intensities in Mössbauer diffractometry of materials with complex Mössbauer energy spectra. The kinematical theory seems adequate for explaining diffraction intensities in these samples having small effective crystallite sizes and a distribution of nuclear resonance energies.

ACKNOWLEDGMENTS

This work was supported by the U. S. National Science Foundation under Contract No. DMR-9816617.

TABLE I. Numbers of backscattered photons from the multislice calculation.

Photon category	$^{57}Fe_3Al$ 0Al condition	$^{57}Fe_3Al$ 4Al condition	bcc $^{57}Fe_3Al$ x-ray only
starting photons	100%	100%	100%
coherent x-ray	0.1463%	0.1391%	0.2246%
incoherent x-ray	0.0285%	0.0275%	0.0364%
recoilless Mössbauer	1.8500%	1.9743%	
nonrecoilless Mössbauer	0.6153%	0.6785%	

APPENDIX A: MULTISLICE CALCULATIONS AND RESULTS

This section describes ''multislice'' computer calculations of the numbers of different photons that were transmitted through, and scattered from, a sequence of thin layers (''slices'') of material. These multislice calculations were used to determine a value for r_{MX} for Eq. (19). Our multislice calculations were performed without considering the effects of coherent interference. Fortunately, r_{MX} was large, and trends in the interference effect calculations with Eq. (9) were not sensitive to the particular value of r_{MX} when r_{MX} was large. The multislice calculations also determined which photon interactions are significant enough to warrant tracking, indicating if a kinematical scattering theory is adequate.

Only the 14.41 keV source photons were tracked though the various slices of sample and back to the surface. Both the recoilless and nonrecoilless 14.41 keV photons from the source were considered, as diffraction peaks include both x-ray and Mössbauer components. The different 14.41 keV photons are scattered by these processes: (1) nonrecoilless from source, coherent x-ray Rayleigh scattering; (2) nonrecoilless from source, incoherent x-ray scattering; (3) recoilless from source, coherent x-ray Rayleigh scattering; (4) recoilless from source, incoherent x-ray scattering; (5) recoilless from source, Mössbauer absorption, recoillessly reemitted (coherent); and (6) recoilless from source, Mössbauer absorption, nonrecoillessly reemitted (incoherent). While only the coherently scattered photons contribute to diffraction peaks, the incoherent scattering adds to the background of the diffraction pattern, so we tracked the incoherent scattering too. Double scattering processes, such as (3) from above leading to (5) or vice versa, were found to be secondary effects that can be ignored.

In the multislice calculation, photons that do not interact in a slice were propagated to the next. The non-recoilless source photons interact with the material through x-ray processes only. X-ray absorption is primarily due to photoelectric absorption. These absorbed photons were not considered further. On the other hand, photons scattered coherently and incoherently by x-ray processes were tracked back to surface of the sample. Absorption of these backscattered photons was allowed, but additional scatterings were found to be unimportant. If the backscattered x-ray scattered photons were not absorbed, they were counted as scattered photons of the appropriate type.

The recoilless source photons may undergo either x-ray or Mössbauer processes. Mössbauer-absorbed (resonant) photons were further categorized by the method of subsequent nuclear decay: recoilless reemission, nonrecoilless reemission, and internal conversion. The backscattered recoilless reemitted photons were attenuated through both Mössbauer and x-ray absorption; the nonrecoilless, by x-ray processes only. The nonrecoillessly reemitted photons were treated as incoherently scattered Mössbauer photons. (A more thorough calculation could include the thermal scattering of these photons that contribute to a varying background under the diffraction pattern.) If the reemitted photons were not absorbed, they were counted as scattered Mössbauer photons of the appropriate type. We did not consider further the products of the other decay channels of the ^{57}Fe nucleus, i.e., internal conversion decays such as Auger electrons and Fe x rays.

The multislice calculation for $D0_3$ $^{57}Fe_3Al$ samples consists of two separate calculations, one each for the 0Al and 4Al environments. The following data were used: (1) $^{57}Fe_3Al$ composition, (2) 95% ^{57}Fe enrichment, (3) 5 to 7 micron sample thickness, (4) 7.02 g/cm^3 density, (5) 5.72×10^{-8} cm layer thickness (3 Fe and 1 Al atoms), and (6) a recoil free fraction of 0.80. The inverse lengths for scattering and absorption for the $^{57}Fe_3Al$ are (1) coherent x-ray scattering 4.77 cm^{-1}, (2) incoherent x-ray scattering 0.77 cm^{-1}, (3) total x-ray absorption 365 cm^{-1}, (4) total Mössbauer absorption 122,400 cm^{-1}, (5) 0Al Mössbauer absorption 1,432 cm^{-1}, and (6) 4Al Mössbauer absorption 1,665 cm^{-1}. The x-ray scattering data are from Ref. 46. The calculation was found to provide consistent nesults with as few as 25 slices of 400 layers each (0.23 microns).

Absorption of backscattered photons was significant, resulting in a ~30% decrease in the scattering intensity. Double scattering processes were determined to be negligible. Double scattered Mössbauer photons amount to only 3% of the single scattered photons and similarly for the x-ray photons.

Table I presents the results for the calculated percentages for the coherent x-ray, incoherent x-ray, recoillessly reemitted Mössbauer, and nonrecoillessly reemitted Mössbauer scattering. X-ray scattering is suppressed by about 35% when both Mössbauer and x-ray events were allowed to occur. The Mössbauer absorption removes photons that would have otherwise undergone x-ray scattering. The Mössbauer to x-ray scattering ratio r_{MX} can be estimated from the coherent scattering results reported in Table I.

[1] P. J. Black and P. B. Moon, Nature (London) **188**, 481 (1960).

[2] P. J. Black, G. Longworth, and D. A. O'Conner, Proc. Phys. Soc. London **83**, 925 (1964).

[3] D. A. O'Conner and P. J. Black, Proc. Phys. Soc. London **83**, 941 (1964).

[4] J. G. Mullen, A. Djedid, B. Bullard, G. Schupp, D. Cowan, Y. Cao, M. L. Crow, and W. Yelon, Hyperfine Interact. **40**, 123 (1988).

[5] R. A. Wagoner, J. G. Mullen, and G. Schupp, Phys. Rev. C **47**, 1951 (1993).

[6] J. G. Mullen, R. A. Wagoner, and G. Schupp, Hyperfine Interact. **83**, 147 (1994).

[7] G. Faigel and M. Tegze, Hyperfine Interact. **92**, 1137 (1994).

[8] M. Tegze and G. Faigel, Hyperfine Interact. **92**, 1143 (1994).

[9] R. A. Wagoner and J. G. Mullen, Phys. Rev. B **49**, 12 425 (1994).

[10] P. P. Kovalenko, V. G. Labushkin, A. K. Ovsepyan, R. Sarkisov, G. V. Smirnov, and I. G. Tolpekin, Zh. Éksp. Teor. Fiz. **88**, 1336 (1985) [Sov. Phys. JETP **61**, 793 (1985)].

[11] Y. Nakai, M. Hirano, Y. Ooi, and N. Kunitomi, J. Phys. Soc. Jpn. **51**, 929 (1982).

[12] Y. Nakai, Y. Ooi, and N. Kunitomi, J. Phys. Soc. Jpn. **57**, 3172 (1988).

[13] P. J. Black and I. P. Duerdoth, Proc. Phys. Soc. London **84**, 169 (1964).

[14] Yu. Kagan and A. M. Afanasev, *Proceedings of the International Atomic Energy Agency Symposium on Mössbauer Spectroscopy and its Applications* (IAEA, Vienna, 1972), p. 143.

[15] V. A. Belyakov, Usp. Fiz. Nauk **115**, 553 (1975) [Sov. Phys. Usp. **18**, 267 (1975)].

[16] U. van Bürck, Hyperfine Interact. **27**, 219 (1986).

[17] G. V. Smirnov, Hyperfine Interact. **27**, 203 (1986).

[18] H. de Waard, Hyperfine Interact. **68**, 143 (1991).

[19] G. V. Smirnov, Hyperfine Interact. **72**, 63 (1992).

[20] G. V. Smirnov and A. I. Chumakov, in *Resonant Anomalous X-ray Scattering*, edited by G. Materlik, C. J. Sparks, and K. Fisher (Elsevier, Amsterdam, 1994), p. 604.

[21] E. Gerdau, R. Rüffer, H. D. Rüter, and J. P. Hannon, Hyperfine Interact. **40**, 49 (1988).

[22] J. Arthur, D. E. Brown, S. L. Ruby, G. S. Brown, and G. K. Shenoy, J. Appl. Phys. **67**, 5704 (1990)

[23] R. Rüffer, Synchrotron Radiat. News **5**, 25 (1992).

[24] E. Gerdau and U. van Bürck, in *Resonant Anomalous X-ray Scattering*, edited by G. Materlik, C. J. Sparks, and K. Fisher (Elsevier, Amsterdam, 1994), p. 589.

[25] U. van Bürck *et al.*, Phys. Rev. Lett. **59**, 355 (1987).

[26] G. V. Smirnov, Hyperfine Interact. **97/98**, 551 (1996).

[27] G. T. Trammell, *Proceedings of the International Atomic Energy Agency Symposium on Chemical Effects of Nuclear Transformations*, Prague, 1960 (IAEA, Vienna, 1961), Vol. 1, p. 75.

[28] A. M. Afanasev and Yu. Kagan, Pisma Zh. Eks. Teor. Fiz. **2**, 130 (1965) [JETP Lett. **2**, 81 (1965)].

[29] Yu. Kagan, A. M. Afanasev, and V. G. Kohn, J. Phys. C **12**, 615 (1979).

[30] J. P. Hannon and G. T. Trammell, Phys. Rev. **186**, 306 (1969).

[31] J. P. Hannon and G. T. Trammell, Physica B **159**, 161 (1989).

[32] A. M. Afanasev and Yu. Kagan, Zh. Éksp. Teor. Fiz. **52**, 191 (1967) [Sov. Phys. JETP **25**, 124 (1967)].

[33] U. Van Bürck, G. V. Smirnov, R. L. Mössbauer, and Th. Hertrich, J. Phys.: Condens. Matter **2**, 3989 (1990).

[34] T. A. Stephens, W. Keune, and B. Fultz, Hyperfine Interact. **92**, 1095 (1994).

[35] B. Fultz and J.M. Howe, *Transmission Electron Microscopy and Diffractometry of Materials* (Springer-Verlag, Heidelberg, 2001), Sec. 1.5.1.

[36] J. M. Cowley, *Diffraction Physics* (North-Holland, Amsterdam, 1975), Sec. 5.3.

[37] U. van Bürck, G. V. Smirnov, R. L. Mössbauer, F. Parak, and N. A. Semioschkina, J. Phys. C **11**, 2305 (1978).

[38] U. Kriplani, J. Y. Y. Lin, M. Regehr, and B. Fultz, Phys. Rev. B (to be published).

[39] J. Arthur, G. S. Brown, D. E. Brown, and S. L. Ruby, Phys. Rev. Lett. **63**, 1629 (1989).

[40] J. J. Bara, Phys. Status Solidi A **58**, 349 (1980).

[41] J. Ballon, V. Comparat, and J. Pouxe, Nucl. Instrum. Methods **217**, 213 (1983).

[42] T. A. Stephens, Ph.D. Thesis, California Institute of Technology, 1996.

[43] G. Le Caër and J. M. Dubois, J. Phys. E **12**, 1083 (1979).

[44] B. Fultz and Z.-Q. Gao, Nucl. Instrum. Methods Phys. Res. B **76**, 115 (1993).

[45] Z.-Q. Gao and B. Fultz, Philos. Mag. B **67**, 787 (1993).

[46] W. J. Veigele, in *Practical Handbook of Spectroscopy*, edited by J. W. Robinson (CRC Press, Boca Raton, 1991), p. 41.